Supplementary Information

Co^0 anchored on Co/N co-doped porous carbon material inducing H migration to accelerate sulfite oxidation and Hg(II) adsorption in flue gas desulfurization

Tieyue Qi[a,b], Tong Li[a,b,c], Jingzhao Zhang[a,b,d], Linsu Zhu[a,b], Shanlong An[a,b], Lei Xing [a,b], Lidong Wang[a,b,*] and Qiangwei Li [a,b]

a Hebei Key Laboratory of Power Plant Flue Gas Multi-Pollutants Control, Department of Environmental Science and Engineering, North China Electric Power University, Baoding, 071003, China

b MOE Key Laboratory of Resources and Environmental Systems Optimization, College of Environmental Science and Engineering, North China Electric Power University, Beijing, 102206, China

c State Power Investment Corporation Shandong Energy Development Co., LTD., Jinan, 250000, China

d China Nuclear Power Engineering Co., LTD, Hebei Branch, Shijiazhuang 050000, China

** Corresponding authors: Lidong Wang*

E-mail address: wld@tsinghua.edu.cn

Submitted to

Journal of Materials Chemistry A

Number of pages (including this page): 29

Number of texts: 5

Number of figures: 10

Number of tables: 12

Texts

Text S1. Reagent and materials.

Cobalt nitrate hexahydrate ($Co(NO_3)_2 \cdot 6H_2O$, AR, purity ≥ 98.5%) and methanol (MeOH, AR, purity ≥ 99.5%) were purchased from Komio Chemical Reagents (China); zinc nitrate hexahydrate ($Zn(NO_3)_2 \cdot 6H_2O$, AR, purity ≥ 99.0%) was purchased from Damao Chemical Reagent. 2-methylimidazole (2-MeIm, AR, purity ≥ 98%); $(NH_4)_2SO_3$ (AR, purity ≥ 92%) was purchased from McClean Chemical Reagents (China). Cobalt powder (Co, AR, ≥ 99.0%) and barium chloride ($BaCl_2$, AR, purity ≥ 99.5%) were purchased from Tianjin Institute of Chemical Reagents (China). A mercury standard solution (1000 $\mu g \cdot mL^{-1}$) was purchased from national standard testing and certification company (China). All reagents were used without further purification.

Text S2. Characterization.

Scanning electron microscopy (SEM: geminiSEM300, ZEISS, Germany) and high-resolution transmission electron microscopy (HRTEM: JEM-2100F, JEOL, Japan) were used to observe the morphology and structure of the prepared catalyst. The chemical composition and crystal phase composition of the catalyst were determined by an X-ray diffraction analysis (XRD: D8 Advance, Bruker, Germany). X-ray photoelectron spectroscopy (XPS: ESCALAB 250 XI, Thermo Fisher Scientific, USA) was used to analyse the valence states and chemical bonds of the various elements in the catalyst. The specific surface area, pore size and pore volume of the catalyst were measured using an adsorption analyser (ASAP 2460, Micromeritics, USA). The Brunauer-Emmett-Teller (BET) equation was used to calculate the specific surface area of the sample, and the Barrett-Joyner-Halenda (BJH) desorption equation was used to calculate the pore size distribution of the sample. The sample was pre-treated at 200°C. X-ray absorption fine structure (XAFS) measurements were performed at the beamline of the Beijing Synchrotron Radiation Facility. The chemical bonds inside the catalyst were determined using a Fourier transform infrared (FT-IR) spectrometer (Nicolet iZ10, Thermo Fisher Scientific, USA). The content of each material element was determined by inductively coupled plasma optical emission spectrometry (ICP-OES: PE7000DV, USA). The formation of free radicals in the reaction was detected by electron spin resonance (ESR: A300, Brooke, Germany). The content of C, N, O in synthesized material was obtained by using an elemental analyser (EA: vario micro, Elementar, Germany).

Text S3. Reusability of Co^0@Co-N-C

In order to investigate the stability of Co^0@Co-N-C in sulfite oxidation and Hg(II) adsorption, the cyclic experiments of $(NH_4)_2SO_3$ oxidation and Hg(II) adsorption by using Co^0@Co-N-C were conducted, with results shown in Fig. S3 and S4. The Co^0@Co-N-C was recovered by filtration and drying after each reaction cycle. And the cyclic sulfite catalytic oxidation and Hg(II) adsorption experiments were conducted under the same experimental conditions as exhibited in section 2.3 and 2.4. It can be seen that the $(NH_4)_2SO_3$ oxidation rate gradually decreased to 0.0663 $mmol \cdot L^{-1} \cdot s^{-1}$ along with the cycle numbers, which is still being 5.53 times that of the non-catalytic oxidation rate. This may be caused by the catalyst loss during the recovery process and the partial consumption of active Co in sulfite catalytic oxidation. And the cyclical performance of Co^0@Co-N-C in adsorbing Hg(II) was displayed in Fig. S4. It can be seen that the removal efficiency of Hg(II) decreased from 98.16% to 82.10% after four cycles, which is still acceptable compared to other materials. To further investigate its structural stability of Co^0@Co-N-C, the XRD was used to compare its composition before and after 4 cycles reaction. From Fig.S5, the diffraction peaks corresponding to Co^0 were weakened to a certain extent, which may be due to its partly participation during sulfite catalytic oxidation. Whereas, the Co^0 peak can be still clearly observed which can ensure the high Hg(II) adsorption performance of the used Co^0@Co-N-C. Therefore, the Co^0@Co-N-C material features an acceptable stability in both sulfite oxidation and Hg(II) adsorption.

Text S4. Analysis of N 1s and C 1s XPS spectra of Co^0@Co-N-C before and after the reaction

The comparison of N 1s XPS spectra of Co^0@Co-N-C before and after the reaction was shown in Fig. S8. The peak intensity of pyridine-N in Co^0@Co-N-C decreased after the catalysis reaction and also the catalysis/adsorption. This may be due to the acceleration of electron transfer by pyridine-N of Co^0@Co-N-C, thereby promoting the catalytic reaction. At the same time, the Co-N_x peak intensity increased significantly, which further enhanced the activation effect of Co-N_x. Fig. S9 shows a comparison of the C 1s spectra of Co^0@Co-N-C before and after the reaction. It shows that there were no significant changes in XPS C 1s before and after the catalytic oxidation of $(NH_4)_2SO_3$ and the catalytic oxidation of $(NH_4)_2SO_3$ combined with Hg(II) adsorption, indicating the strong structural stability of Co^0@Co-N-C. All the above XPS analysis results were consistent with the results of the above experiments and the XRD characterization analysis, i.e., the coupling effect of the uniformly dispersed Co^0 particles in the Co^0@Co-N-C material and the Co-N_x structure achieves the catalytic oxidation of $(NH_4)_2SO_3$.

Text S5. Kinetics and isotherm analysis for Hg(II) adsorption

To evaluate the adsorption capacity of the Co^0@Co-N-C material for Hg(II), an adsorption kinetics test was conducted for 120 min. The results revealed that Co^0@Co-N-C could rapidly remove large amounts of Hg(II) within 40 min, and the reaction reached an adsorption equilibrium in about 120 min. The pseudo-first-order kinetic model, pseudo-second-order kinetic model, intraparticle diffusion model and Elovich kinetic model were used to fit the experimental data of Hg(II) adsorption kinetics. Fig. S6(a) shows the kinetic fitting curve of Hg(II) adsorption by Co^0@Co-N-C, and Table S6 gives the relevant parameters of the adsorption kinetic fitting curve. The Hg(II) adsorption kinetic results were consistent with the Elovich model, with a correlation coefficient (R^2) of 0.9908. This result indicates that the adsorption of Hg(II) by the Co^0@Co-N-C catalyst occurred through chemical adsorption. To determine the maximum saturated adsorption capacity and adsorption mechanism of Co^0@Co-N-C for Hg(II), Langmuir, Freundlich, Temkin and Dubinin-Radushkevich (D-R) adsorption models were used to fit the adsorption isotherm curve of Co^0@Co-N-C for Hg(II). From the fitting results shown in Fig. S6(b) and Table S7, it can be seen that the Langmuir adsorption model had the highest fitting degree to the Hg(II) adsorption data of Hg(II), with an R^2 value of 0.9970. The saturated adsorption capacity fitted according to the Langmuir model was 210.4 $mg \cdot g^{-1}$, which was similar to the saturated adsorption capacity of 267.76 $mg \cdot g^{-1}$ obtained in the experiment. Therefore, it was speculated that the Hg(II) adsorption process on the Co^0@Co-N-C surface followed a monolayer adsorption mechanism with uniform adsorption sites.

Figures

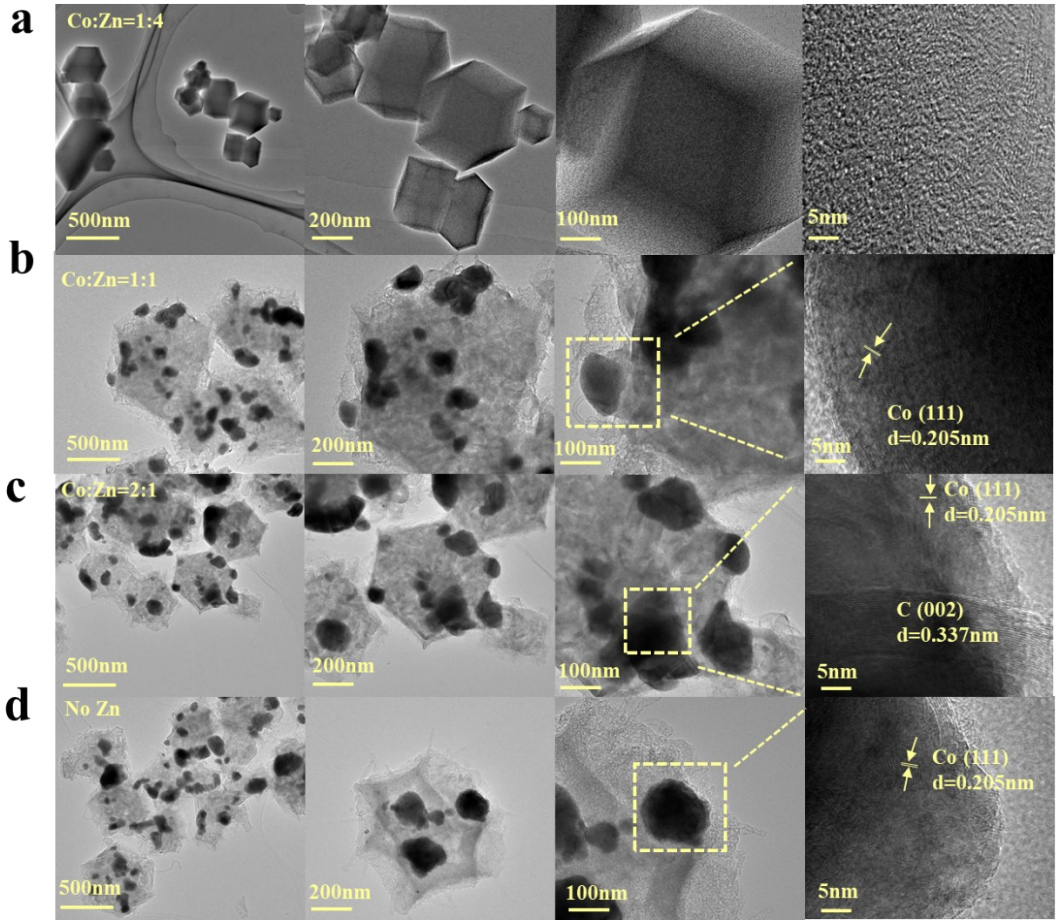

Fig. S1. HRTEM images of different Co/Zn ratios. a Co: Zn=1:4, b Co: Zn=1:1, c Co: Zn=2:1, d No Zn.

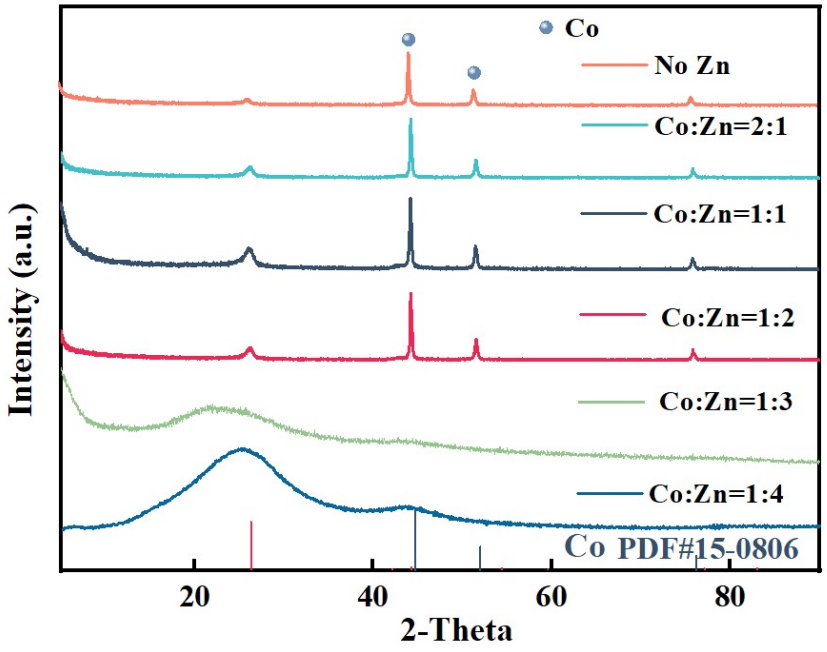

Fig. S2. Wide-angle XRD patterns of synthesized material with different Co/Zn ratios

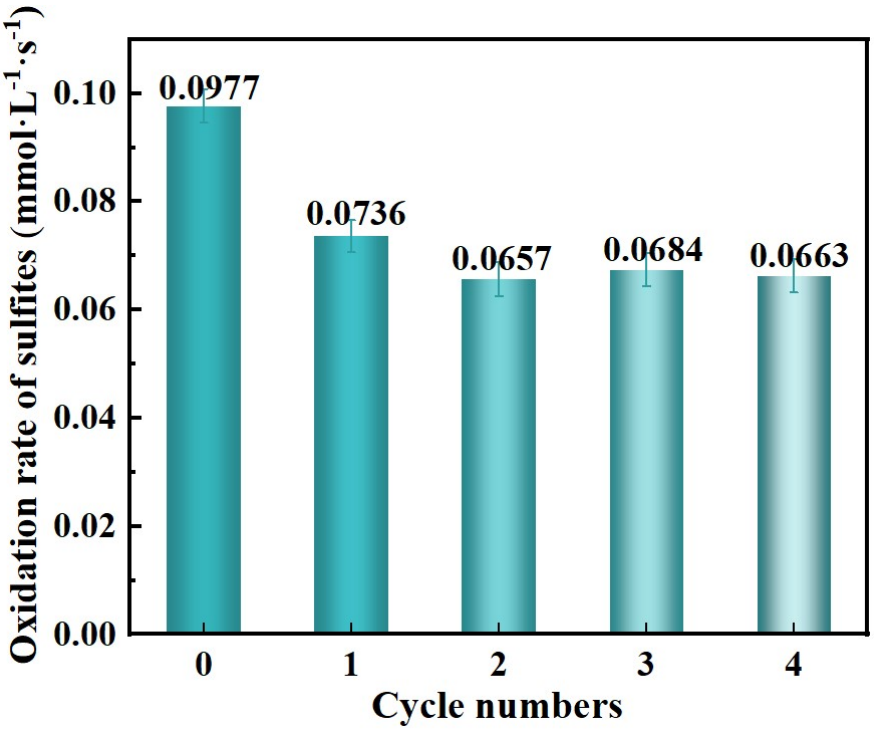

Fig. S3. Catalytic sulfite oxidation cycle experiment using Co^0@Co-N-C

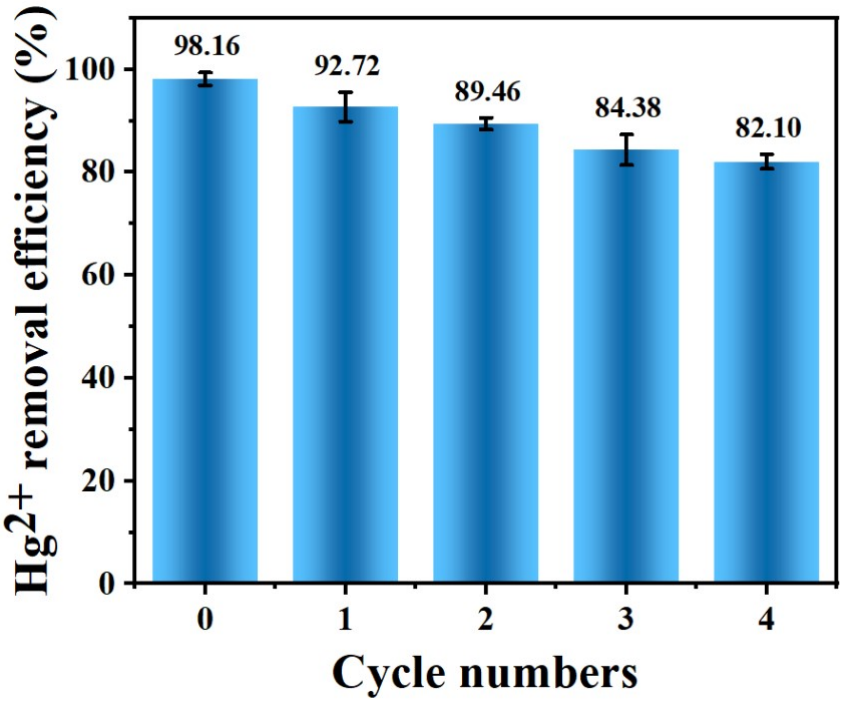

Fig. S4. Hg (II) adsorption cycle experiment using Co^0@Co-N-C

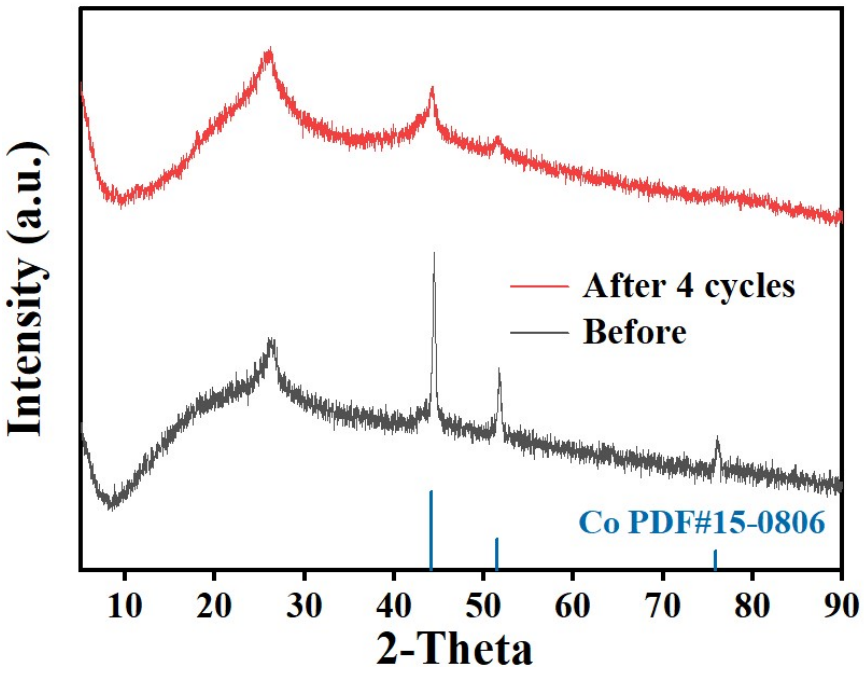

Fig. 5. XRD pattern of Co^0@Co-N-C material before and after reaction

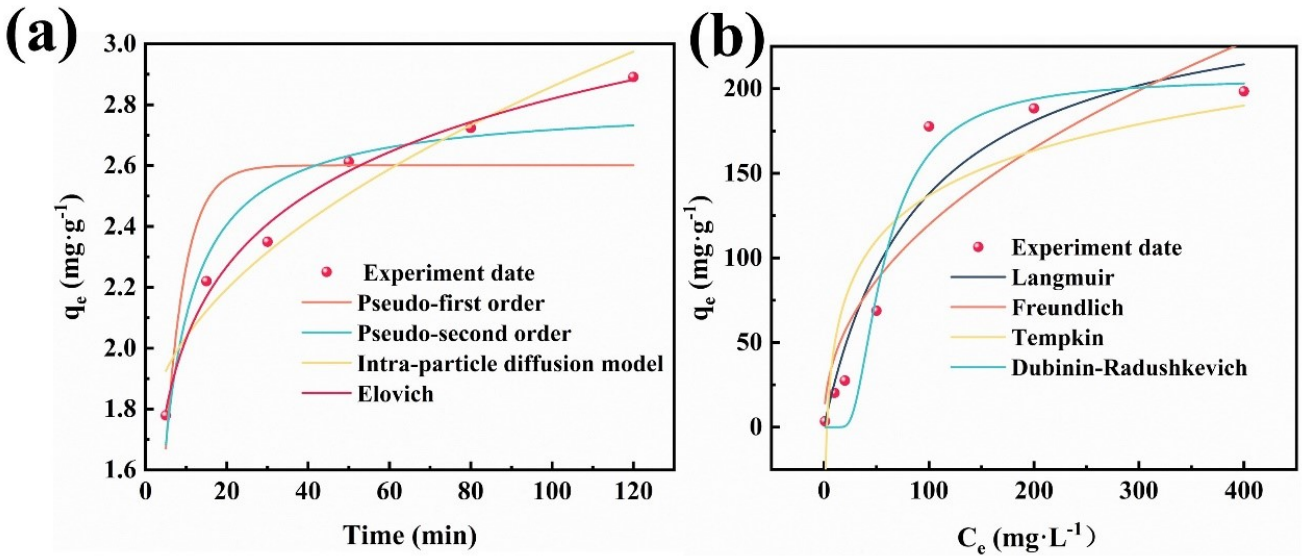

Fig. S6.(a) The kinetic model fitting curve of Hg (II) adsorption by Co^0@Co-N-C.(b)The isothermal model fitting curve of Hg (II) adsorption by Co^0@Co-N-C.

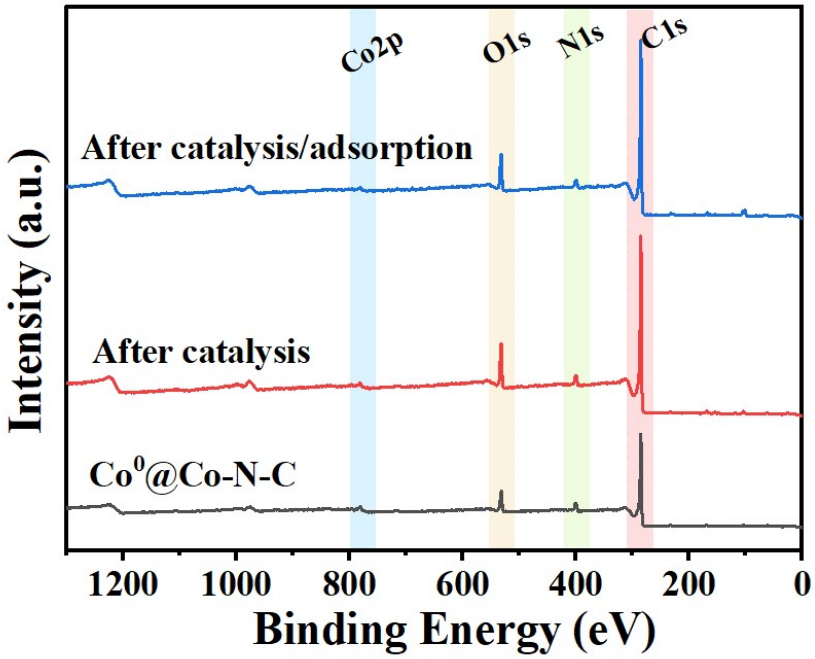

Fig. S7. XPS survey analysis of Co^0@Co-N-C before and after reaction

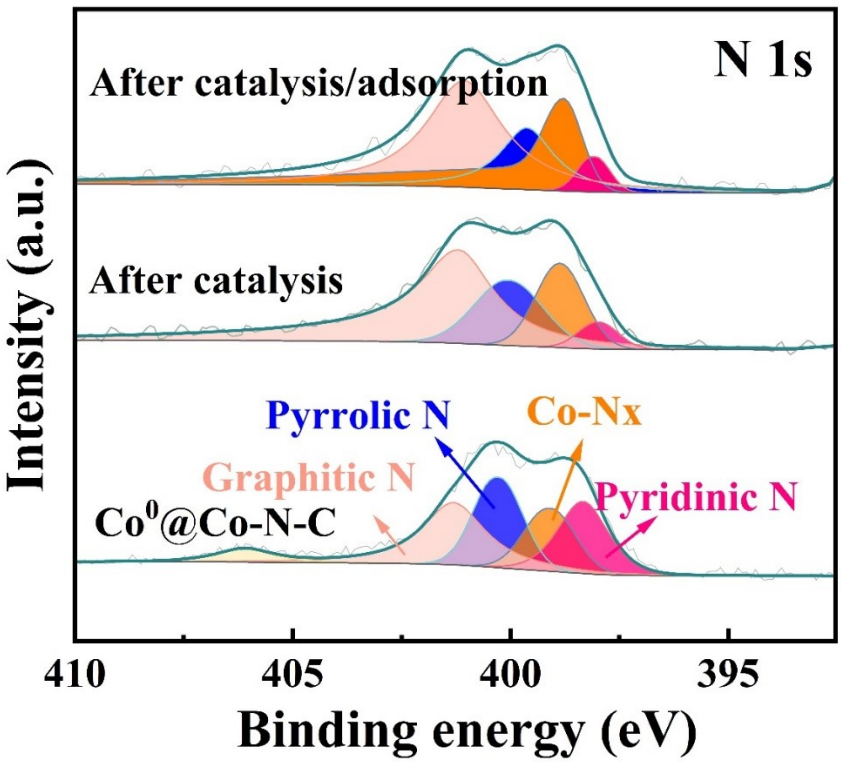

Fig. S8. N 1s XPS spectra of Co^0@Co-N-C before and after reaction

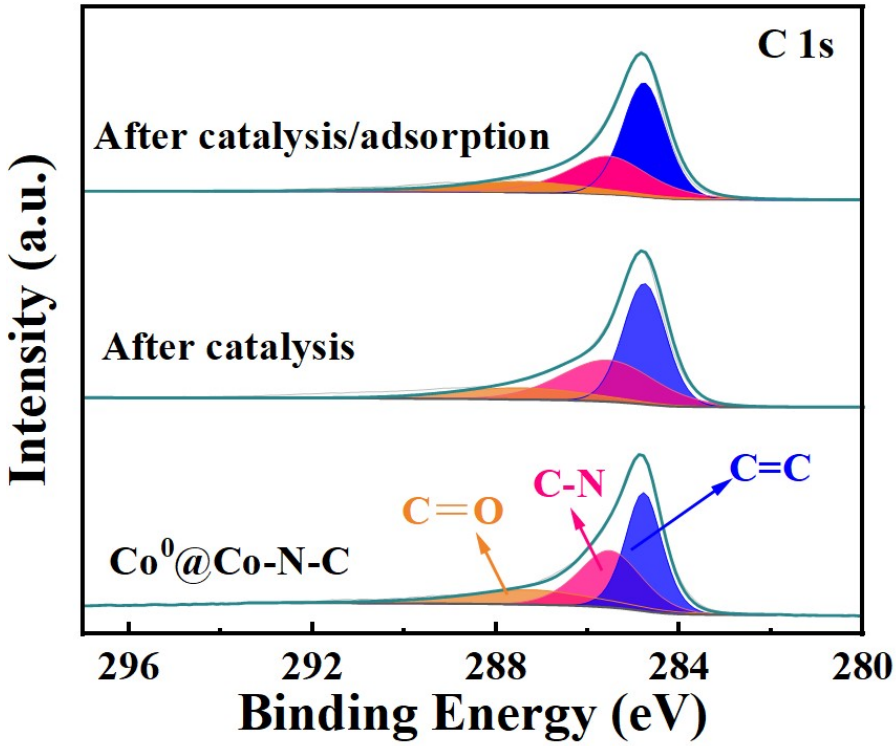

Fig. S9. C 1s XPS spectra of Co^0@Co-N-C before and after reaction

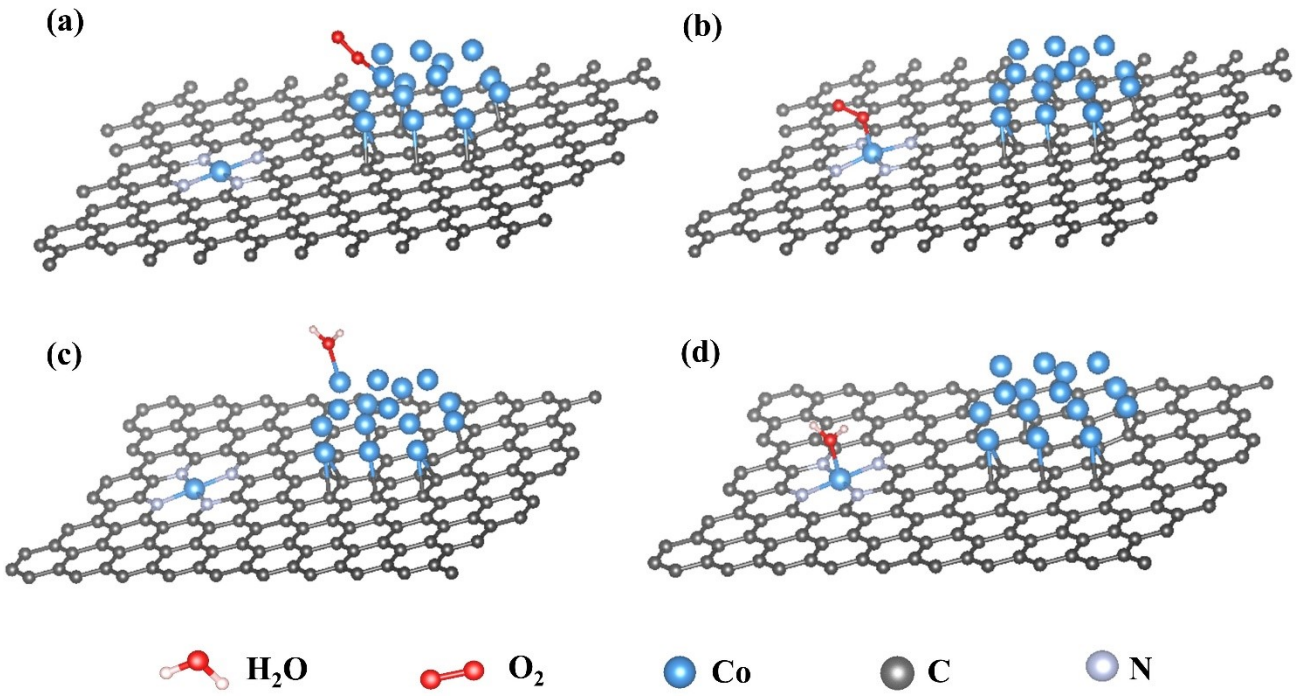

Fig. S10. (a) The adsorption configurations of O_2 on Co^0 site of Co^0@Co-N-C, (b) The adsorption configurations of O_2 on Co-N site of Co^0@Co-N-C, (c) The adsorption configurations of H_2O on Co^0 site of Co^0@Co-N-C, (d) The adsorption configurations of H_2O on Co-N site of Co^0@Co-N-C

Tables

Table S1. Cobalt content of synthesized materials obtained by ICP

Co:Zn	Co content, wt%
1:4	1.59
1:2	10.40
1:1	27.26
2:1	42.03
No Zn	56.03

Table S2. The elemental analysis results of Co^0@Co-N-C

Elements	C	O	N
Contents	77%	10%	3%

Table S3. The physical properties of materials with different cobalt-zinc ratios

Co:Zn	specific surface area ($m^2 \cdot g^{-1}$)	pore volume ($cm^3 \cdot g^{-1}$）	average pore size (nm)
1:4	573.78	0.38	2.43
1:3	392.29	0.29	3.23
1:2	254.69	0.28	4.31
1:1	110.04	0.18	6.77

Table S4. Cobalt proportion of Co^0@Co-N-C with different Co-Zn ratio from XPS analysis

Materials	Co^0/Co	Co-N_x/Co
Co:Zn=1:1	33.47	66.53
Co:Zn=1:2	16.54	83.46
Co:Zn=1:4	0	100

Table S5. Oxygen proportion of Co^0@Co-N-C with different Co-Zn ratio from XPS analysis

Materials	adsorbed oxygen (O_β, %)	lattice oxygen (O_α, %)	O_β/O_α
Co:Zn=1:1	70.06	29.94	2.34
Co:Zn=1:2	87.32	12.68	6.89
Co:Zn=1:4	64.34	35.66	1.80

Table S6. Performance comparison of Co^0@Co-N-C with reported catalysts and adsorbents for sulfite catalytic oxidation and Hg(II) adsorption

Materials	Sulfite oxidation rate (mmol/L/s)	Catalyst dose (g/L)	Hg^{2+} Removal capacity (mg/g)	Ref.
Co-MCM-48	0.074	0.5	\	[1]
Co_3O_4-NPs@KIT-6	0.090	1	\	[2]
Mn@ZIF67	0.077	0.5	\	[3]
Co/Mn–Ac	0.055	1	\	[4]
Co_3O_4 NCs/g-C_3N_4	0.073	1	\	[5]
N/S-MCMs/Fe_3O_4	\	\	74.5	[6]
MWCNT-AA	\	\	101.35	[7]
Co-CNTs	0.069	0.5	166.7	[8]
Co-TUD-1/S	0.083	2	96	[9]
Co^0@Co-N-C	**0.098**	**0.25**	**267.8**	This work

Table S7. The kinetic model fitting results of Hg (II) adsorption by Co^0@Co-N-C

kinetic model	R^2	Other related parameters
Pseudo-first-order kinetic model	0.7020	q_e =2.60 mg·g^{-1}，K_1=0.31
Pseudo-second order kinetics model	0.9096	q_e =2.81 mg·g^{-1}，K_2=0.11
Intraparticle diffusion model	0.9377	K_2=0.12，c=1.66
Elovich model	0.9908	α = 12.85 g·mg^{-1}，β=1.66

Table S8. Isothermal model fitting results of Hg (II) adsorption on Co^0@Co-N-C

Adsorption isotherm model	R^2	Other related parameters
Langmuir	0.9970	q_m=267.76 mg·g^{-1}，K_L=0.008
Freundlich	0.9662	K_F=11.30，N=2.066
Temkin	0.8918	A=0.31，b=65.05
Dubinin-Radushkevich	0.9486	q_m=200.58 mg·g^{-1}，K_{dr}=5.35×10^{-4}，E=30.57

Table S9. Cobalt proportion of Co^0@Co-N-C before and after reaction obtained from XPS

Materials	Co^0, %	Co-N_x, %
Co^0@Co-N-C	16.54	83.46
After catalysis	15.74	84.26
After catalysis / adsorption	13.28	86.72

Table S10. Oxygen proportion of Co^0@Co-N-C before and after reaction obtained from XPS

Materials	adsorbed oxygen (O_β, %)	lattice oxygen (O_α, %)	O_β / O_α
Co^0@Co-N-C	87.32	12.68	6.89
After catalysis	54.58	45.42	1.20
After catalysis / adsorption	49.69	50.31	0.99

Table S11. Cobalt proportion changes on surface of Co^0@Co-N-C obtained by in-situ XPS

specimen	Co^0, %	Co-N_x, %
0min	45.12	54.88
$O_2$15min	35.19	64.81
H_2O15min	33.10	66.90

Table S12. Oxygen proportion changes on surface of Co^0@Co-N-C obtained by in-situ XPS

Materials	adsorbed oxygen (O_β, %)	lattice oxygen (O_α, %)
0min	43.30	56.70
$O_2$15min	59.32	40.68
H_2O15min	55.09	44.91

References

1 L. Wang, L. Xing, J. Liu, T. Qi, S. Zhang, Y. Ma and P. Ning, *Chem. Eng. J.*, 2021, **407**, 127210.

2 T. Qi, L. Wang, Y. Wang, L. Xing and S. Zhang, *Environ. Sci. Technol.*, 2019, **53**, 13477–13485.

3 L. Xing, J. Liu, T. Qi, L. Wang, Z. Wang and S. Zhang, *Appl. Catal. B*, 2020, **275**, No.119143.

4 J. Liu, S. Lu, L. Wang and Qi.Tieyue, *J. Hazard. Mater.* , 2018, **365**, 531-537.

5 J. Liu, H. Wang, L. Wang, L. Xing, S. Zhang, H. Xiao and Y. Ma, *Chem. Eng. Sci.*, 2019, **197**, 1-10.

6 M. Liu, X. Deng, D. Zhu, H. Duan, W. Xiong, Z. Xu and L. Gan, *Chinese Chem. Lett.*, 2016, **27**, 795-800.

7 A.K. Singha Deb, V. Dwivedi, K. Dasgupta, S. Musharaf Ali and K. T. Shenoy, *Chem. Eng. J.*, 2016, **313**, 899-911.

8 L. Wang, T. Qi, M. Hu, S. Zhang, P. Xu, D. Qi, S. Wu and H. Xiao, *Environ. Sci. Technol.*, 2017, **51**, 11346-11353.

9 L. Zhang, L. Xing, J. Liu, T. Qi, M. Li and L. Wang, *Sep. Purif. Technol.*, 2021, **266**, 118546.